UV and Visible Raman Studies of Oxygen Vacancies in Rare-Earth-Doped Ceria

ARTICLE *in* LANGMUIR · MARCH 2011

Impact Factor: 4.46 · DOI: 10.1021/la200292f · Source: PubMed

5 AUTHORS, INCLUDING:

Jiqing Lu
Zhejiang Normal University
124 PUBLICATIONS **2,387** CITATIONS
SEE PROFILE

Mengfei Luo
Zhejiang Normal University
75 PUBLICATIONS **1,267** CITATIONS
SEE PROFILE

Langmuir

ARTICLE

pubs.acs.org/Langmuir

UV and Visible Raman Studies of Oxygen Vacancies in Rare-Earth-Doped Ceria

Ming Guo, Jiqing Lu, Yanni Wu, Yuejuan Wang, and Mengfei Luo*

Key Laboratory of the Ministry of Education for Advanced Catalysis Materials, Institute of Physical Chemistry, Zhejiang Normal University, Jinhua 321004, China

Supporting Information

ABSTRACT: Surface properties of rare-earth (RE) doped ceria (RE = Sm, Gd, Pr, and Tb) were investigated by UV (325 nm) and visible (514, 633, and 785 nm) Raman spectroscopy, combined with UV−vis diffuse reflectance spectroscopy, high-resolution transmission electron microscopy, and X-ray photoelectron spectra techniques. It was found that the optical absorption property of samples, the wavelength of detecting laser line, and the inhomogeneous distribution of the dopants significantly affected the obtained surface information, namely, the peak intensity and shape at ca. 460 and 570 cm^{-1}, as well as the observed oxygen vacancy concentration (A_{570}/A_{460}). The UV laser line detected the surface information of RE-doped ceria and disclosed the presence of many oxygen vacancies in the samples. The visible laser lines penetrated into the inner layer of the Sm- or Gd-doped CeO_2 and reflected the whole information of samples because of their weak absorptions of the visible laser. However, the Pr- or Tb-doped CeO_2 absorbed visible light strongly; thus, the laser can only determine the outer surface information of the sample.

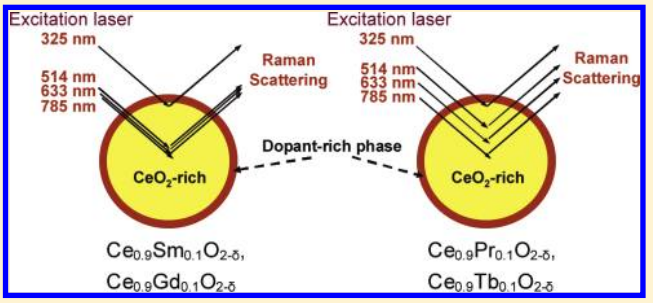

1. INTRODUCTION

In the past decade, modification of ceria with rare-earth (RE) elements, such as La, Pr, Sm, Gd, Tb, Er, and Nd, has been widely applied in the field of catalysis and solid oxide fuel cells.[1−4] Many of these applications benefit from the presence of oxygen vacancy defects due to the insertion of RE ions into the CeO_2 lattice, as it confers unusual properties to RE-doped ceria compared with CeO_2.[5,6] Therefore, much research was carried out to investigate the effect of these dopants on the amount, mobility, and distribution state of oxygen vacancies in CeO_2-based materials.[7,8]

Recently, Chen et al. proposed that formation of stable defects on the surface of ceria was unlikely under ambient conditions.[9] Besides, Ou et al.[10] and Esch et al.[11] suggested that the presence of excessive oxygen vacancies in pure or RE-doped ceria would lead to the formation of vacancy clustering/ordering, which may block the mobility of oxygen vacancies and have negative influence on the catalytic and conductive properties of the samples subsequently. Interestingly, Liu and co-workers pointed out that the presence of oxygen vacancy clustering facilitated the activation and transportation of active oxygen species, thus promoting the reducibility and activity of ceria nanorods.[12] Also, the oxygen vacancy clustering may dissociate to free oxygen vacancies under practical conditions and promote the conductive property of Sm- and/or Nd-doped ceria.[13] So a better understanding of the influence of the type of dopants on the resulting CeO_2 materials requires a detailed analysis.

Raman spectroscopy has been used to detect the oxygen vacancies and proven to be a very powerful characterization technique.[14] In this paper, UV (325 nm) and visible (514, 633, and 785 nm) Raman laser lines were employed to obtain reliable information, because one excitation laser line may provide possible ambiguities in the structural information of the sample.[15] The main objective of this work is to investigate the relationship between Raman spectra and the optical absorbance properties of RE-doped ceria in ambient conditions, such as Pr- or Tb-doped dark sample and Sm- or Gd-doped light sample. We will also discuss the possible distribution state of doping elements, which would be helpful to understand the reaction of many important chemical processes.

2. EXPERIMENTAL SECTION

2.1. Material Preparation. CeO_2 and $Ce_{0.9}RE_{0.1}O_{2-\delta}$ (RE = Sm, Gd, Pr, and Tb) samples were prepared by a sol−gel method. $Ce(NO_3)_3 \cdot 6H_2O$ (99.9%) and the corresponding metal oxides (Sm_2O_3, Gd_2O_3, Pr_6O_{11}, Tb_4O_7, 99.9%) were used as precursors. $Ce(NO_3)_3 \cdot 6H_2O$ and citrate with the amount of the total moles of metal ions were dissolved by deionized H_2O. The aqueous metal nitrate (obtained by dissolving metal oxide with HNO_3) was added dropwise to the above solutions under stirring conditions. Consequently, the mixture was heated at 90 °C with stirring until it became a viscous gel. Then the gel was dried at 120 °C overnight, and then calcined at 900 °C for 4 h to obtain the final material. The practical value of RE components is ca. 9.8% (atomic ratio), as determined by an X-ray fluorescence (XRF) technique, which is very close to the nominal value.

2.2. Characterizations. X-ray diffraction (XRD) patterns were collected on a PANalytical X'Pert PRO MPD powder diffractometer

Received: September 16, 2010
Published: March 11, 2011

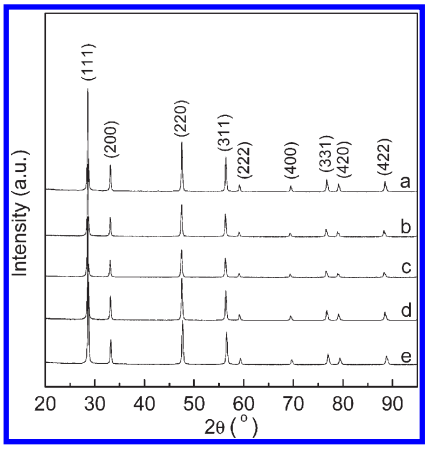

Figure 1. XRD patterns of (a) CeO_2 and (b) Sm-, (c) Gd-, (d) Pr-, and (e) Tb-doped CeO_2.

using Cu Kα radiation and operating at 40 kV and 40 mA. The lattice parameters of the samples were determined by the Rietveld method, and the average crystallite sizes were calculated by full curve fitting, using JADE 6.5 software. High-resolution transmission electron microscopy (HRTEM) images were obtained using a JEOL-2100F microscope operating at 120 kV.

Specific surface areas of the samples were determined by a multipoint Brunauer−Emmett−Teller (BET) analysis of the nitrogen adsorption and desorption isotherms at liquid nitrogen temperature recorded on an Autosorb-1 apparatus. Prior to analysis, the samples were heated at 120 °C in vacuum for 6 h.

X-ray photoelectron spectra (XPS) were recorded on a Kratos Axis Ultra DLD spectrometer using Al Kα radiation (1486.6 eV) as the excitation source. The analysis was performed at room temperature. Binding energies were calibrated by using the containment carbon (C 1s = 284.6 eV). Semiquantitative analysis of atomic ratio was accomplished by determining the elemental peak areas.

Ultraviolet−visible (UV−vis) diffuse reflectance spectra were performed under ambient conditions using a Nicolet Evolution 500 spectrophotometer equipped with an integrating sphere. $BaSO_4$ was used as a reference, and spectra were recorded in the range of 200−800 nm.

Raman spectra were collected by a Renishaw RM1000 confocal microprobe under ambient conditions. The excitation wavelengths were 325, 514, 633, and 785 nm. The power of each laser line was kept at about 3 mW to prevent a local heating effect, and the resolution of the spectrometer was 1 cm^{-1} with the diameter of the analyzed spot being ca. 1 μm. The sample was always pretreated in N_2 at 500 °C for 1 h and then cooled down to room temperature under flowing N_2 before each measurement.

3. RESULTS AND DISCUSSION

Figure 1 shows the XRD patterns of CeO_2 and Sm-, Gd-, Pr-, and Tb-doped CeO_2. The diffraction peaks of all the samples could be indexed to (111), (200), (311), (222), (400), (331), (420), and (422) crystal faces, corresponding to the fluorite structure of CeO_2. Besides, no diffraction peaks of RE oxides are observed, indicating that $Ce_{0.9}RE_{0.1}O_{2-\delta}$ solid solutions may be formed.

The lattice parameters of CeO_2 and $Ce_{0.9}RE_{0.1}O_{2-\delta}$ samples, with the number in parentheses indicating the analytical error, are listed in Table 1. It is found that the lattice parameters of the RE-doped ceria are different from that of CeO_2, further

Table 1. Lattice Parameter (a), Average Crystallite Size (D), BET Surface Area (S), and Ce/RE Atomic Ratio of CeO_2 and $Ce_{0.9}RE_{0.1}O_{2-\delta}$ Samples

sample	a^a (nm)	D^a (nm)	S (m^2 g^{-1})	Ce/RE atomic ratio^b
CeO_2	0.5412(2)	52.2	11.6	—
$Ce_{0.9}Sm_{0.1}O_{2-\delta}$	0.5423(2)	50.1	15.0	5.25
$Ce_{0.9}Gd_{0.1}O_{2-\delta}$	0.5418(2)	43.5	19.1	5.67
$Ce_{0.9}Pr_{0.1}O_{2-\delta}$	0.5413(1)	31.3	16.9	3.17
$Ce_{0.9}Tb_{0.1}O_{2-\delta}$	0.5395(2)	42.5	17.7	2.85

^{a} From XRD analysis. ^{b} From XPS analysis.

confirming the formation of solid solutions. Chen et al.[9] suggested that the lattice change of ceria is closely related to the crystallite size, the oxygen vacancy concentration, and the analysis conditions. So, for RE-doped ceria, the change of lattice parameter resulted from the substitution of cerium by rare-earth cations may also need to be taken into consideration.

The radii of Sm^{3+} (0.108 nm) and Gd^{3+} (0.105 nm) cations are larger than that of Ce^{4+} (0.097 nm),[16] so the substitution of Ce^{4+} by Sm^{3+} or Gd^{3+} cations will cause an expansion of the lattice. Also, Pr^{3+} (0.113 nm) and Tb^{3+} (0.104 nm) cations have larger ionic radius than that of Ce^{4+}, while the radii of Pr^{4+} (0.096 nm) and Tb^{4+} (0.088 nm) cations are smaller than that of Ce^{4+}. Thus, Pr^{4+} might also have a larger proportion in the solid solution. Besides, the existence of oxygen vacancies would expand the lattice of ceria according to the literature.[9] It is clear that all of the RE-doped ceria show lattice expansion resulting from the substitution and oxygen vacancies complex effect, except for Tb-doped ceria. The smaller lattice parameter of $Ce_{0.9}Tb_{0.1}O_{2-\delta}$ (0.5395 nm) suggested that a negative substitution effect surpasses the oxygen vacancy expanding effect, indicating the presence of many Tb^{4+} cations in the solid solution. As for the crystallite size, it is clear that the average crystallite size of RE-doped ceria is smaller than that of pure CeO_2 (Table 1), as determined by XRD analysis, which indicates that additive may prevent crystallite growth.[17,18] Consequently, the smaller crystallite size of the doped CeO_2 results in a higher surface area, as shown in Table 1. Moreover, all the samples have a high degree of crystallinity, and small or amorphous particles were not observed (Figure SI 1, Supporting Information). Thus, the lattice contraction effect due to an increase of surface tension caused by the presence of an amorphous particle can be ignored. Table 1 also lists the surface atomic ratio of Ce and RE in the $Ce_{0.9}RE_{0.1}O_{2-\delta}$ samples obtained by XPS analysis using the sensitivity factor method. It is found that the RE (Sm, Gd, Pr, and Tb) contents are higher than the nominal composition (10%), which suggested that the distribution of RE dopants was inhomogeneous in the samples.[19,20] The small decrease of crystallite size of RE-doped ceria may be caused by additive segregating at the grain surfaces.

Figure 2 shows the HRTEM images of the doped CeO_2 samples. It is found that the particles exhibit irregular shapes, and the average particle size of the samples ranges from 30 to 50 nm (Figure SI 1, Supporting Information), which is in agreement with the XRD analysis (Table 1). A close check of Figure 2 reveals that the particles mainly expose thermodynamically stable (111) faces, and small fraction of (200) faces was also observed. Besides, the clearly visible parallel lattice fringes give proof of a high degree of crystallinity. The lattice spacing of the (111) face

dx.doi.org/10.1021/la200292f |*Langmuir* 2011, 27, 3872–3877

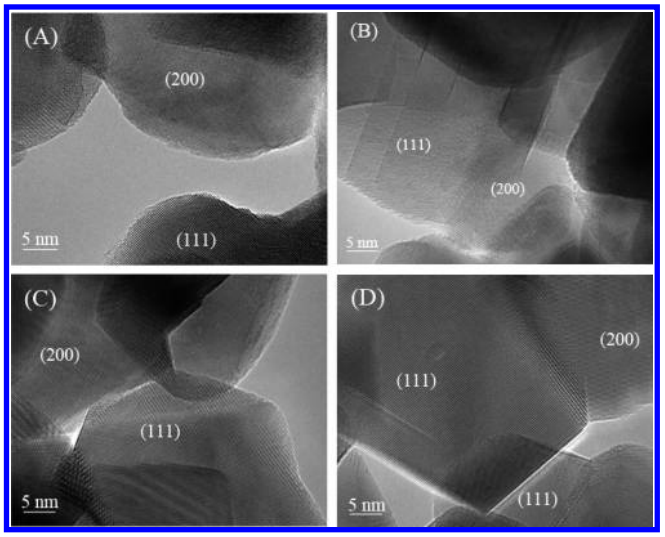

Figure 2. HRTEM images of (A) Sm-, (B) Gd-, (C) Pr-, and (D) Tb-doped CeO_2.

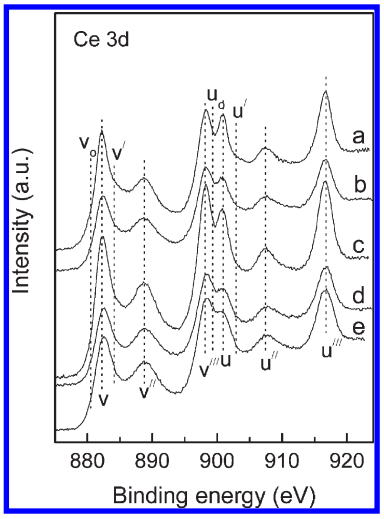

Figure 3. Ce 3d XPS patterns of (a) CeO_2 and (b) Sm-, (c) Gd-, (d) Pr-, and (e) Tb-doped CeO_2.

of Sm-, Gd-, Pr-, and Tb-doped ceria is 0.3412, 0.3135, 0.3127, and 0.3100 nm, respectively.

The composition and chemical states of Ce and RE ions in the samples were examined by the XPS technique. The Ce 3d XPS patterns of CeO_2 and Sm-, Gd-, Pr-, and Tb-doped CeO_2 are shown in Figure 3. The XPS pattern of the Ce $3d_{5/2}$ will be composed of two structures of Ce_2O_3 and three structures of CeO_2. However, if we take into account of spin−orbit coupling, 10 peaks should be analyzed. The bands v_o, v, v′, v″, and v‴ are attributed to the Ce $3d_{5/2}$ ionization, while u_o, u, u′, u″, and u‴ are assigned to Ce $3d_{3/2}$ ionization. The bands labeled v, v″, v‴, u, u″, and u‴ belong to Ce^{4+} ions, and the bands labeled v_o, v′, u_o, and u′ are assigned to Ce^{3+} ions.[21,22] It is clear that Ce^{4+} and Ce^{3+} coexisted on the surface of all the samples, and the major valence of cerium is 4+ oxidation, because the relative concentration of Ce^{3+} and Ce^{4+} are in relative proportion to the intensity of corresponding peaks. The peak areas of Ce^{3+}/total areas ratio were used to calculate the relative amount of Ce^{3+}.[22]

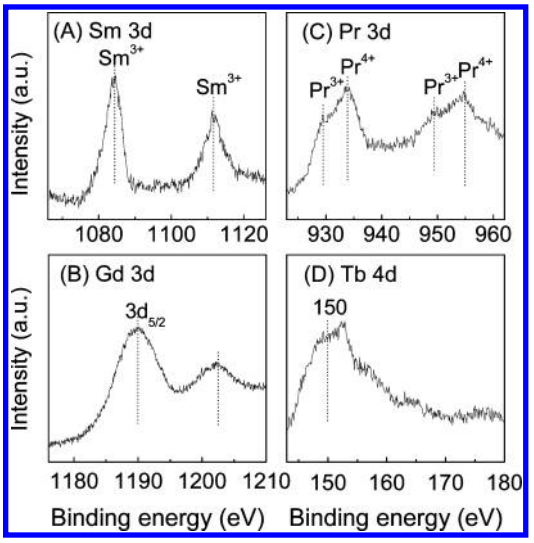

Figure 4. (A) Sm 3d, (B) Gd 3d, (C) Pr 3d, and (D) Tb 4d XPS patterns of Sm-, Gd-, Pr-, and Tb-doped CeO_2.

However, it is difficult to obtain a concrete value due to the complex backgrounds.

Figure 4 shows the Sm 3d, Gd 3d, Pr 3d, and Tb 4d XP spectra of the RE-doped CeO_2. Two bands at binding energies of ca. 1084 and 1111 eV are observed in Figure 4 A, which are attributed to the $3d_{5/2}$ and $3d_{3/2}$ ionization of Sm^{3+}, respectively.[23] The Gd 3d photoemission spectrum (Figure 4B) shows typical peaks in the range from 1175 to 1210 eV for Gd $3d_{5/2}$, which is in agreement with the literature.[24] Two sets of spin−orbit multiples are observed at ca. 954 and 934 eV in Figure 4C, which represent the $3d_{5/2}$ and $3d_{3/2}$ ionization of Pr, respectively. Besides, the signals at ca. 929.5 and 949.4 eV are assigned to Pr^{3+}, and the signals at ca. 954.3 and 933.9 eV are attributed to Pr^{4+}.[22] So Pr^{3+} and Pr^{4+} may coexist in the sample, and major oxidation state of Pr is Pr^{4+}, according to the peak intensity. However, the XP spectra of Tb oxidation were rarely reported, while there is agreement that Tb^{3+} gives a signal below 150 eV and the characteristic features of Tb^{4+} are above 150 eV.[25,26] We concluded that Tb may exist in both trivalence and tetravalence because the spectrum shows a maximum peak at ca. 152 eV accompanied by apparent shoulders below 150 eV and a long tail above 150 eV.

UV−vis diffuse reflectance spectroscopy has been used to study various metal oxides to obtain information on the surface coordination and different oxidation states of the metal ions. Figure 5 shows the UV−vis diffuse reflectance spectra of CeO_2 and $Ce_{0.9}RE_{0.1}O_{2-\delta}$ samples. As can be noted from this figure, the major UV−vis absorption for spectrum of CeO_2 occurs at about 255, 285, and 340 nm. The former maxima (255 nm) correspond to O^{2-} to Ce^{3+} charge transfer transitions, whereas the latter two absorption maxima may be caused by O^{2-} to Ce^{4+} charge transfer (285 nm) and interband (340 nm) transitions.[27]

In general, the formation of a solid solution not only alters the crystallinity but also affects the charge transfer properties and optical characteristics of the resulting samples. For the Sm- or Gd-doped ceria, strong absorption is observed in the UV region (<400 nm), while there is merely no increase in the visible region (>450 nm) compared with that of CeO_2. The concentration of Ce^{3+} ions is in relative proportion to the intensity of ultraviolet absorption peak. So, the increase of absorption in the UV region indicates that the substitution of Ce^{4+} with RE ions indeed

dx.doi.org/10.1021/la200292f |Langmuir 2011, 27, 3872–3877

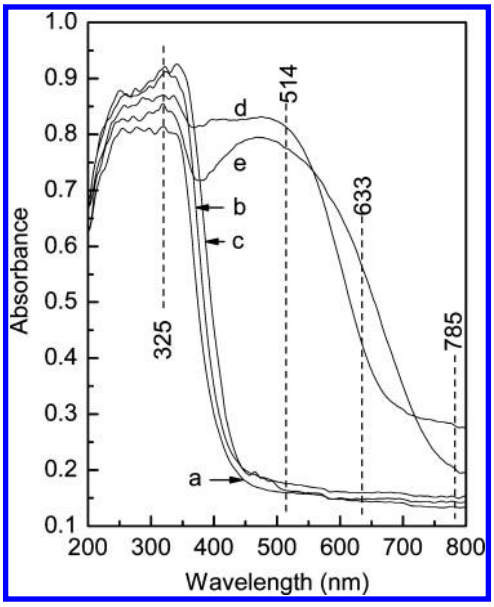

Figure 5. UV−vis diffuse reflectance spectra of (a) CeO_2 and (b) Sm-, (c) Gd-, (d) Pr-, and (e) Tb-doped CeO_2.

facilitates the formation of Ce^{3+}, which will increase the oxygen vacancy concentration of Ce-based materials due to a charge compensation mechanism.[28] However, doping CeO_2 with Pr or Tb shows obvious absorption from 200 to 800 nm, and the absorption intensity becomes weaker with increasing wavelength, following the order of 325 nm > 514 nm > 633 nm > 785 nm.

The Raman spectra of Sm- and Pr-doped CeO_2 obtained under ambient conditions with four different excitation laser lines (325, 514, 633, and 785 nm) are shown in Figure 6. For the $Ce_{0.9}Sm_{0.1}O_{2-\delta}$ sample, when a visible excitation laser line is used, one intense band at ca. 460 cm^{-1} and two weak bands at ca. 546 and 600 cm^{-1} are observed. The 460 cm^{-1} band is attributed to the Raman-active vibrational mode (F_{2g}) of fluorite-type structure. It can be viewed as a symmetrical stretching vibration of the oxygen atoms around cerium ions.[29] The 546 cm^{-1} band could be assigned to oxygen vacancies introduced into the ceria in order to maintain charge neutrality when Ce^{4+} ions are replaced with trivalent cations. Besides, the 600 cm^{-1} band is ascribed to the intrinsic oxygen vacancies due to the presence of Ce^{3+} of ceria nanopowder, which can be observed obviously in Raman spectrum of CeO_2 with 325 nm excitation laser line.[30,31] However, as the UV laser line (325 nm) is used, the bands at 546 and 600 cm^{-1} merge as a broad band and the band at 460 cm^{-1} is much weaker compared with that using a visible laser line. For the $Ce_{0.9}Pr_{0.1}O_{2-\delta}$ sample, the band at 460 cm^{-1} becomes weaker with decreasing wavelength of the laser line, and a broad band centered at ca. 570 cm^{-1} is observed.

Figure 6 clearly demonstrates the changing trends of Raman bands of the same sample with different excitation laser lines, which results from the absorption properties of the samples. The band at 460 cm^{-1} is weak when the 325 nm laser line is used, which is due to the strong absorption of the samples in the UV region (Figure 5). When the sample absorbs the excitation laser strongly, the majority of excitation laser and scattering light are absorbed by sample and only partial light carrying surface information can escape from the absorption.[32] Therefore, the intensity of the band at 460 cm^{-1} is weak. As the excitation laser line increases its wavelength (from UV to visible region), the laser increases its sampling depth of the sample.[33] As the light colored

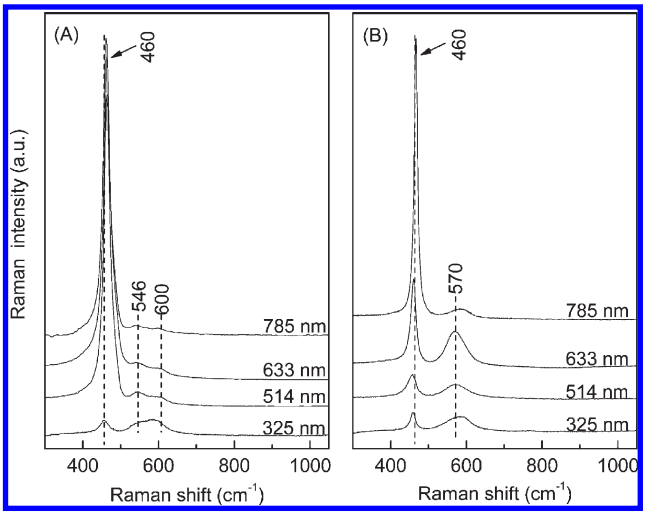

Figure 6. Raman spectra of (A) Sm- and (B) Pr-doped CeO_2 at 325, 514, 633, and 785 nm excitation laser lines.

$Ce_{0.9}Sm_{0.1}O_{2-\delta}$ shows weak absorption in the visible region, the laser line penetrates into a deeper layer of the sample and all the information of the sample is obtained, which makes the band at 460 cm^{-1} stronger. However, $Ce_{0.9}Pr_{0.1}O_{2-\delta}$ shows quite intense absorption in the visible region and its intensity decreases with increasing wavelength; the intensity of the band at 460 cm^{-1} gradually becomes stronger, indicating that the sampling depth increases with wavelength. Therefore, various excitation laser lines should be used at the same time to obtain accurate and overall information of the samples during Raman experiments.

As the Raman spectra of $Ce_{0.9}Gd_{0.1}O_{2-\delta}$ and $Ce_{0.9}Tb_{0.1}O_{2-\delta}$ samples are almost identical to those of $Ce_{0.9}Sm_{0.1}O_{2-\delta}$ and $Ce_{0.9}Pr_{0.1}O_{2-\delta}$ samples, respectively, the spectra are not presented.

Figure 7 shows the Raman spectra of Sm-, Gd-, Pr-, and Tb-doped CeO_2 with different excitation laser lines. It is found that all the samples show similar spectra when the 325 nm laser line is used, namely, a sharp F_{2g} Raman band of ceria (460 cm^{-1}) and a broad oxygen vacancy band (570 cm^{-1}). When the visible laser lines are used, $Ce_{0.9}Sm_{0.1}O_{2-\delta}$ and $Ce_{0.9}Gd_{0.1}O_{2-\delta}$ samples show one strong band at ca. 460 cm^{-1} and two weak oxygen vacancy bands at ca. 546 and 600 cm^{-1}. However, $Ce_{0.9}Pr_{0.1}O_{2-\delta}$ and $Ce_{0.9}Tb_{0.1}O_{2-\delta}$ samples show a weaker band at 460 cm^{-1} and a stronger band at ca. 570 cm^{-1}.

This suggests that the doping of ceria with different RE cations may induce different types of oxygen vacancy under the same excitation laser line. It is well-known that the RE ions, including Ce, easily form a series of nonstoichiometric oxides of the type REO_x, where $1.5 \leq x \leq 2$. However, neither Pr nor Tb tends to crystallize in the dioxide or sesquioxide phases; they would rather form compounds with Pr_6O_{11} and Tb_4O_7. Maybe that is why doping ceria with Pr or Tb has a unique optical absorbance property compared with other RE-doped ceria.

Considering the characteristic bands of oxygen vacancies (546 and 600 cm^{-1} for $Ce_{0.9}Sm_{0.1}O_{2-\delta}$ or $Ce_{0.9}Gd_{0.1}O_{2-\delta}$, and 570 cm^{-1} for $Ce_{0.9}Pr_{0.1}O_{2-\delta}$ or $Ce_{0.9}Tb_{0.1}O_{2-\delta}$), they are strong under the 325 nm laser line but weak under visible laser lines. This is also due to the fact that the sampling depth increases with increasing laser line wavelength and oxygen vacancies enrich at the surface of the sample, so the concentration of surface oxygen vacancies of the sample is obviously higher than that of its internal layer. Therefore, the observed oxygen vacancy intensity

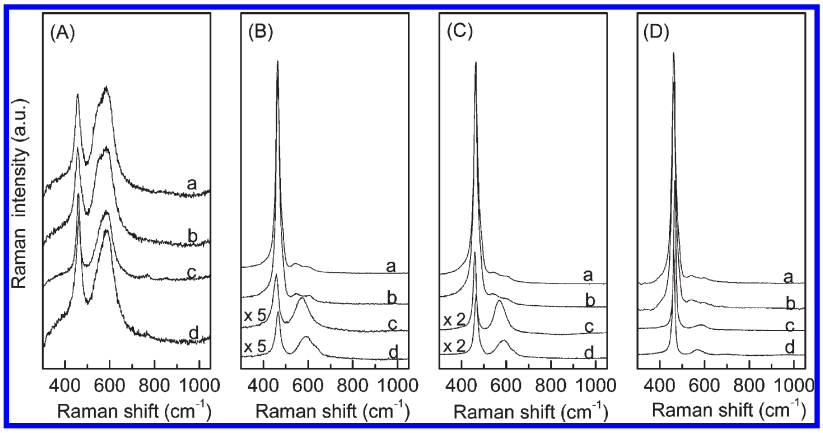

Figure 7. Raman spectra of (a) Sm-, (b) Gd-, (c) Pr-, and (d) Tb-doped CeO_2 at (A) 325 nm, (B) 514 nm, (C) 633 nm, and (D) 785 nm excitation laser lines.

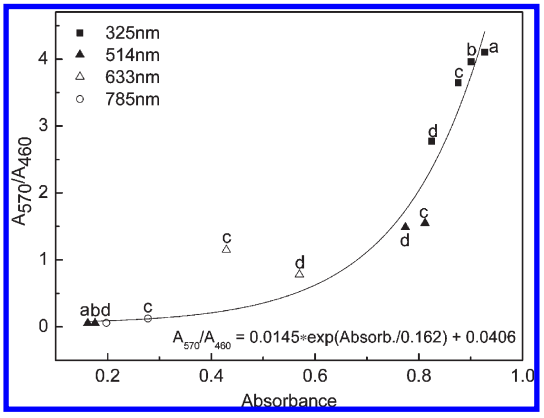

Figure 8. Relationship between A_{570}/A_{460} and absorbance of (a) Sm-, (b) Gd-, (c) Pr-, and (d) Tb-doped CeO_2 with different excitation laser lines.

of the samples decreases along with the increase of laser wavelength. If $Ce_{0.9}Pr_{0.1}O_{2-\delta}$ or $Ce_{0.9}Tb_{0.1}O_{2-\delta}$ further decreases its absorption of the laser line, such as the 1064 nm laser line, the laser should penetrate into a deeper layer of sample and reflect the whole information, just like the Sm- or Gd-doped ceria. Therefore, the weaker oxygen vacancy intensity and two types of oxygen vacancies would be observed.[34,35]

The ratio of integral intensity of the band of oxygen vacancies and of the F_{2g} mode of fluorite-type structure [A_{570}/A_{460}, for $Ce_{0.9}Sm_{0.1}O_{2-\delta}$ or $Ce_{0.9}Gd_{0.1}O_{2-\delta}$ samples is $(A_{546} + A_{600})/A_{460}$] reflects the relative oxygen vacancy concentration. This ratio as a function of absorbance of samples is listed in Figure 8. It is found that the ratio increases with increasing absorbance of samples, following an exponential order. This is due to the fact that the samples have strong absorption and only partial light carrying surface information escapes in the UV region; thus, the UV-Raman spectra reflect the outer surface information of samples. When the visible laser line is used, the inner layer information of the sample is obtained, because of the deeper penetration of the laser. Therefore, the doping RE contents may decrease rapidly from the outer surface to the inner layer of samples. Borchert et al.[22] also pointed out that the Pr content decreased rapidly from the outer to the internal surface of the $Pr_xCe_{1-x}O_{2-y}$ mixed oxide, indicating that the oxygen vacancy concentration caused by Pr substitution is higher at the outer surface than at the internal layers.

Although numerous studies have been conducted on the RE-doped ceria, the distribution of the dopants in the sample is rarely discussed. In this work, RE-doped CeO_2 are investigated by Raman spectroscopy using various excitation laser lines. The results show that the A_{570}/A_{460} ratio changes with the wavelength due to the different penetrating depth of the laser line (Figure 2), thus implying the inhomogeneous distribution of the dopants in the CeO_2-based samples. By this Raman spectroscopic method, the distribution of the dopants in the CeO_2 could be effectively detected, although the analysis might be qualitative. More importantly, for those light colored samples, such as ceria doped with Sm, Gd, or other RE elements, the investigation of the surface property could be more effective using a short-wavelength laser (e.g., 325 nm) compared with that under visible laser lines. This is because these samples have strong absorption in the UV region, thus the Raman spectra contain more information about the outer surface.

4. CONCLUSIONS

For the inhomogeneous rare-earth-doped ceria, the surface information obtained by Raman spectroscopy was greatly related to the optical absorption property of samples and the wavelength of the detecting laser line. The UV Raman spectra revealed that there are many oxygen vacancies at the surface of the rare-earth-doped ceria. The visible Raman spectra of $Ce_{0.9}Sm_{0.1}O_{2-\delta}$ or $Ce_{0.9}Gd_{0.1}O_{2-\delta}$ contained more bulk information compared to those of $Ce_{0.9}Pr_{0.1}O_{2-\delta}$ or $Ce_{0.9}Tb_{0.1}O_{2-\delta}$ because the former two samples had much weaker absorption of the visible laser line than the latter. The phenomena described in this study must be taken into account to properly interpret the effect of optical absorbance on other information obtained by single Raman laser line, especially for the inhomogeneous material.

■ ASSOCIATED CONTENT

Supporting Information. TEM images of Sm-, Gd-, Pr-, and Tb-doped CeO_2. This material is available free of charge via the Internet at http://pubs.acs.org.

■ AUTHOR INFORMATION

Corresponding Author

*Tel: +86-579-82283910. Fax: +86-579-82282595. E-mail: mengfeiluo@zjnu.cn.

■ ACKNOWLEDGMENT

This work is financially supported by National Natural Science Foundation of China (Grant No. 20873125).

■ REFERENCES

(1) Trovarelli, A. *Catal. Rev. Sci. Eng.* **1996**, *38*, 439.
(2) Steele, B. C. H.; Heinzel, A. *Nature* **2001**, *414*, 345.
(3) Song, Z. X.; Liu, W.; Nishiguchi, H.; Takami, A.; Nagaoka, K.; Takita, Y. *Appl. Catal. A: Gen.* **2007**, *329*, 86.
(4) Krishna, K.; Bueno-López, A.; Makkee, M.; Moulijn, J. A. *Appl. Catal. B: Environ.* **2007**, *75*, 201.
(5) Ganduglia-Pirovano, M. V.; Hofmann, A.; Sauer, J. *Surf. Sci. Rep.* **2007**, *62*, 219.
(6) Ferrizz, R. M.; Wong, G. S.; Egami, T.; Vohs, J. M. *Langmuir* **2001**, *17*, 2464.
(7) Mišta, W.; Małecka, M. A.; Kępiński, L. *Appl. Catal. A: Gen.* **2009**, *368*, 71.
(8) Mori, T.; Buchanan, R.; Ou, D. R.; Ye, F.; Kobayashi, T.; Kim, J.-E.; Zou, J.; Drennan, J. *J. Solid State Electrochem.* **2008**, *12*, 841.
(9) Chen, L.; Fleming, P.; Morris, V.; Holmes, J. D.; Morris, M. A. *J. Phys. Chem. C* **2010**, *114*, 12909.
(10) Ou, D. R.; Mori, T.; Ye, F.; Zou, J.; Auchterlonie, G.; Drennan *J. Phys. Rev. B* **2008**, *77*, 024108.
(11) Esch, F.; Fabris, S.; Zhou, L.; Montini, T.; Africh, C.; Fornasiero, P.; Comelli, G.; Rosei, R. *Science* **2005**, *309*, 752.
(12) Liu, X. W.; Zhou, K.B.; Wang, L.; Wang, B. Y.; Li, Y. D. *J. Am. Chem. Soc.* **2009**, *131*, 3140.
(13) Li, S. P.; Lu, J. Q.; Fang, P.; Luo, M. F. *J. Power Sources* **2009**, *193*, 93.
(14) Schmitt, M.; Popp, J. *J. Raman Spectrosc.* **2006**, *37*, 20.
(15) Fornasiero, P.; Speghini, A.; Monte, R. D.; Bettinelli, M.; Kašpar, J.; Bigotto, A.; Sergo, V.; Graziani, M. *Chem. Mater.* **2004**, *16*, 1938.
(16) Shannon, R. D. *Acta Crystallogr., Sect. A* **1976**, *32*, 751.
(17) Rahaman, M. N.; Zhou, Y. C. *J. Eur. Ceram. Soc.* **1995**, *15*, 939.
(18) Małecka, M. A.; Kępiński, L.; Mišta, W. *J. Alloys Compd.* **2008**, *451*, 567.
(19) Ye, F.; Mori, T.; Ou, D. R.; Zou, J.; Drennan, J. *Mater. Res. Bull.* **2007**, *42*, 943.
(20) Ye, F.; Mori, T.; Ou, D. R.; Zou, J.; Auchterlonie, G.; Drennan, J. *J. Appl. Phys.* **2007**, *101*, 113528.
(21) Romeo, M.; Bak, K.; Fallah, J. E.; Normand, F. L.; Hilaire, L. *Surf. Interface Anal.* **1993**, *20*, 508.
(22) Borchert, H.; Frolova, Y. V.; Kaichev, V. V.; Prosvirin, I. P.; Alikina, G. M.; Lukashevich, A. I.; Zaikovskii, V. I.; Moroz, E. M.; Trukhan, S. N.; Ivanov, V. P.; Paukshtis, E. A.; Bukhtiyarov, V. I.; Sadykov, V. A. *J. Phys. Chem. B* **2005**, *109*, 5728.
(23) Suzuki, K.; Enoki, T.; Bandow, S. *Phys. Rev. B* **1993**, *48*, 11077.
(24) Borchert, H.; Borchert, Y.; Kaichev, V. V.; Prosvirin, I. P.; Alikina, G. M.; Lukashevich, A. I.; Zaikovskii, V. I.; Moroz, E. M.; Paukshtis, E. A.; Bukhtiyarov, V. I.; Sadykov, V. A. *J. Phys. Chem. B* **2005**, *109*, 20077.
(25) Blanco, G.; Pintado, J. M.; Bernal, S.; Cauqui, M. A.; Corchado, M. P.; Galtayries, A.; Ghijsen, J.; Sporken, R.; Eickhoff, T.; Drube, W. *Surf. Interface Anal.* **2002**, *34*, 120.
(26) Li, L.; Wei, Q.; Li, H.; Zhang, D.; Su, W. Z. *Phys. B* **1995**, *96*, 451.
(27) Reddy, B. M.; Bharali, P.; Saikia, P.; Park, S.-E.; van den Berg, M. W. E.; Muhler, M.; Grünert, W. *J. Phys. Chem. C* **2008**, *112*, 11729.
(28) Reddy, B. M.; Bharali, P.; Thrimurthulu, G.; Saikia, P.; Katta, L.; Park, S.-E. *Catal. Lett.* **2008**, *123*, 327.
(29) Keramidas, V. G.; White, W. B. *J. Chem. Phys.* **1973**, *59*, 1561.
(30) McBride, J. R.; Hass, K. C.; Poindexter, B. D.; Weber, W. H. *J. Appl. Phys.* **1994**, *76*, 2435.
(31) Dohčević-Mitrović, Z. D.; Grujić-Brojčin, M.; Šćepanović, M.; Popović, Z. V.; Bošković, S.; Matović, B.; Zinkevich, M.; Aldinger, F. *J. Phys.: Condens. Matter* **2006**, *18*, S2061.
(32) Luo, M. F.; Yan, Z. L.; Jin, L. Y.; He, M. *J. Phys. Chem. B* **2006**, *110*, 13068.
(33) Li, M. J.; Feng, Z. C.; Xiong, G.; Ying, P. L.; Xin, Q.; Li, C. *J. Phys. Chem. B* **2001**, *105*, 8107.
(34) Hungría, A. B.; Martínez-Arias, A.; Fernández-García, M.; Iglesias-Juez, A.; Guerrero-Ruiz, A.; Calvino, J. J.; Conesa, J. C.; Soria, J. *Chem. Mater.* **2003**, *15*, 4309.
(35) Rossignol, S.; Gérard, F.; Mesnard, D.; Kappenstein, C.; Duprez, D. *J. Mater. Chem.* **2003**, *13*, 3017.